Formation and annealing of cubic ice: II. Kinetic study

2008 J. Phys.: Condens. Matter 20 285105

(http://iopscience.iop.org/0953-8984/20/28/285105)

J. Phys.: Condens. Matter **20** (2008) 285105 (14pp) doi:10.1088/0953-8984/20/28/285105

Formation and annealing of cubic ice: II. Kinetic study

T C Hansen[1], M M Koza[1], P Lindner[1] and W F Kuhs[2]

[1] Institut Laue-Langevin, 6 rue Jules Horowitz, BP 156, 38042 Grenoble Cedex, France
[2] Geowissenschaftliches Zentrum der Universität Göttingen, Abteilung Kristallographie, Goldschmidtstraße 1, 37077 Göttingen, Germany

E-mail: hansen@ill.fr

Received 21 January 2008, in final form 30 April 2008
Published 13 June 2008
Online at stacks.iop.org/JPhysCM/20/285105

Abstract

A new structure model (Hansen *et al* 2008 *J. Phys.: Condens. Mater.* **20**) of ice Ic, so-called 'cubic ice'(König 1943 *Z. Kristallogr.* **105** 279), allows the description of the complex diffraction pattern in terms of stacking fault probabilities and anisotropic particle size. To understand the successive transitions when going from metastable recovered high-pressure phases via ice Ic towards the stable ice Ih, as previously observed (Kuhs *et al* 1989 *Z. Kristallogr.* **186** 174, Kuhs *et al* 2004 *Phys. Chem. Chem. Phys.* **6** 4917), two samples of deuterated ice Ic from ice IX and ice V have been studied *in situ* as a function of time at temperatures between 145 and 240 K at the neutron powder diffractometer D20 at ILL. Small changes of stacking fault probability occur hours after formation at about 165 K and continue gradually upon heating towards a higher proportion of hexagonal at the expense of cubic stacking sequences. At 190 K the intensities of the Bragg reflections change considerably and the peaks become sharper. The pattern now increasingly resembles, but does not match exactly, the one of ice Ih until a temperature of about 240 K is reached (Koza *et al* 2005 *Phys. Chem. Chem. Phys.* **7** 1423). We will show quantitatively the time evolution of stacking disorder and crystallite size at different temperatures for ice Ic of different origin obtained from neutron powder diffraction. Small angle neutron scattering with D11 at ILL backs the observations.

1. Introduction

1.1. Background

Ice Ic, so-called 'cubic ice' [2] is a frequent encounter in phase transformations of the water system and is formed in the laboratory by deposition of water vapour at low temperature [2, 6, 7] or by a warming recovered high-pressure phases of ice [8–10]. Ice Ic is also likely to occur in nature: studies of the topology of snowflakes and the ice-crystal growth patterns suggested [11] that some dendrite snowflakes grow from a nucleus of cubic ice. Whalley speculated that water droplets might freeze to cubic ice crystals, as the 28° halo around the sun [12] may have been formed by refraction of light passing through the octahedral crystals of cubic ice in the atmosphere. Riikonen *et al* provided further evidence for airborne cubic ice [13]. More recently, laboratory experiments, in which ice Ic could be formed from micrometre-sized water droplets below 190 K, strongly suggest its presence in the polar stratosphere and tropical tropopause [14–16]. As a metastable phase ice Ic has a higher vapour pressure than ice Ih, thus altering the water vapour distribution and radiative properties of the atmosphere. On the other hand it was argued [17] that the nucleation of ice Ic, its subsequent transformation to ice Ih, and the resulting water vapour differential, would dehydrate the air more efficiently and lead to larger final ice Ih crystals. Not much is known about the kinetics of formation and annealing of ice Ic in this temperature range, which makes a kinetic study by diffraction methods a worthwhile undertaking. A prerequisite for such a study is an appropriate model of the defect structure of ice Ic. Such a model is developed in an accompanying paper [1] and will find application in the following.

Ice Ic is metastable and above 150 K will undergo a transition to hexagonal ice Ih on warming. This transition takes place over a large temperature range, speeding up above 180 to 185 K, and depends on the way the cubic ice was produced. Even at 210 K the transition is not complete but leaves a stacking-faulted hexagonal ice which transforms to pure ice Ih

above 240 K, as shown by *in situ* neutron [4] and *ex situ* x-ray diffraction [15] as well as neutron backscattering [5]. Time-resolved neutron diffraction showed that ice Ic and defective ice Ih is formed even at temperatures above 200 K upon the decomposition of gas hydrates [4]. In sufficiently small mesopores of a few nanometres, ice Ic is stable up to the melting point of ice [18].

1.2. Motivation

In a high-resolution neutron powder diffraction experiment Kuhs *et al* [3] observed a substantial decrease of the width of the 111 reflection of ice Ic (prepared from ice II): a decrease of the width (assumed Lorentzian) by a factor of two in the 155 K to about 180 K region was followed by a slower decrease of further 20% up to 205 K. At this temperature the width related to the instrumental resolution was still not quite reached, but due to limited beam time the case was not followed further. It is interesting to note that a change of relaxation time is also noted at a temperature of about 185 K from heat capacity measurements [19]. From later experiments [4] it seems that with every temperature step new degrees of freedom are accessed leading to a rapid structural change on a timescale of minutes and settling after about one hour in this temperature range. Any detailed structural description of the structural changes upon annealing is still missing. Likewise, the annealing was never followed with a timescale of minutes. Little is understood of the successive release of degrees of freedom when going from a metastable recovered ice, via ice Ic, towards the stable form, normal hexagonal ice (Ice Ih). While it is fairly well established that migrating orientational defects (so-called *Bjerrum* defects [20]) come into play for local relaxation phenomena in the temperature range between 120 and 160 K [21] and persist [22], some probably correlated relaxation phenomena involving several water molecules are increasingly important at higher temperature involving interstitial water molecule diffusion [23], leading possibly to the annealing of stacking faults. However, we do not have any more detailed insight into these processes and the study presented here shall contribute to a further elucidation of this issue.

An important parameter when characterizing ice Ic and its annealing is the particle size. Amongst others Kumai [24] has made observations on the crystal size of vapour-deposited ice Ic by transmission electron microscopy (TEM). He calculates, from the width of the electron diffraction pattern, a mean particle size between 50 and 500 Å increasing with increasing formation temperature; hexagonal ice formed at a higher temperature had significantly larger particle sizes. Again, a systematic study of the temperature-dependency of crystallite size has never been made nor have different cubic ices been compared in this respect. Crystallite sizes have been obtained for cubic ice [25] from the Scherrer formula [26] for small enough crystallites, however, in order to get an independent estimate, also small angle neutron scattering (SANS) was applied. Koza *et al* have studied the transition of HDA/LDA into cubic ice by means of SANS [27, 28] and from this work we know that ice Ic shows indeed a clear SANS signal as well as some T-dependency. Extending this study we now want to follow the evolution of the signal with temperature for two ice Ic samples chosen for their large differences in terms of stacking fault probabilities as well as for their ease of preparation, namely ice IX and ice V.

2. Experimental details

2.1. Sample preparation

The deuterated ice V precursor has been prepared in Grenoble by Koza in a uni-axial high-pressure apparatus under liquid nitrogen. A sample of ice Ih was compressed at 240 to 245 K to 650 MPa nominal pressure and annealed at this condition for 30 min. Subsequently, it has been recovered to ambient pressure at liquid nitrogen temperature.

The deuterated ice IX precursor has been prepared in Göttingen in Bridgman-sealed gas pressure cells [29] under controlled hydrostatic pressure at a controlled temperature in a cold bath following indications given in [30] and [31]: finely crushed Ice Ih was ramped up in pressure from ambient to 300 MPa argon gas pressure in three to four minutes at −60 °C and then quenched immediately in liquid N_2. The sample reached 77 K within two to three minutes. The pressure was released during the quench, the sample recovered and kept in liquid nitrogen.

Another deuterated ice IX precursor was formed by Koza in Grenoble in a uni-axial high-pressure apparatus by following the preparation route of Garg [32]. The temperature and pressure applied during the preparation corresponded with 170–180 K and 1–1.2 GPa, respectively. After formation the sample has been quenched to liquid nitrogen temperature and recovered from the pressure device at ambient pressure. Since this ice IX sample proved to be appreciably strained (anisotropic peak broadening), as evidenced in the diffraction pattern, it was not further analysed.

Earlier comparative work has shown that the kinetics of phase transformations in normal and deuterated solid water systems is not significantly different [33–35]. Thus we can assume that the use of deuterated material does not lead to any loss of generality in our later conclusions.

2.2. Neutron powder diffraction

The *in situ* neutron powder diffraction (NPD) experiments have been conducted at the constant wavelength neutron powder diffractometer D20 [36, 37] at a wavelength of $\lambda = 2.42$ Å, based at the high-flux reactor of the Institut Laue-Langevin (ILL). The instrument was used in its highest flux configuration at a take-off angle of 42° from a vertically focussing highly orientated pyrolytic graphite (HOPG) monochromator. An HOPG filter avoids contamination of the monochromatic beam with $\frac{\lambda}{2}$.

The deuterated ice samples were enclosed inside vanadium sample cans under liquid nitrogen and further kept at controlled temperature inside an *Orange Cryostat*. Both samples have been studied as a function of temperature and time between 145 and 250 K with 5 min data acquisition time per diffraction pattern. The precursors were first held

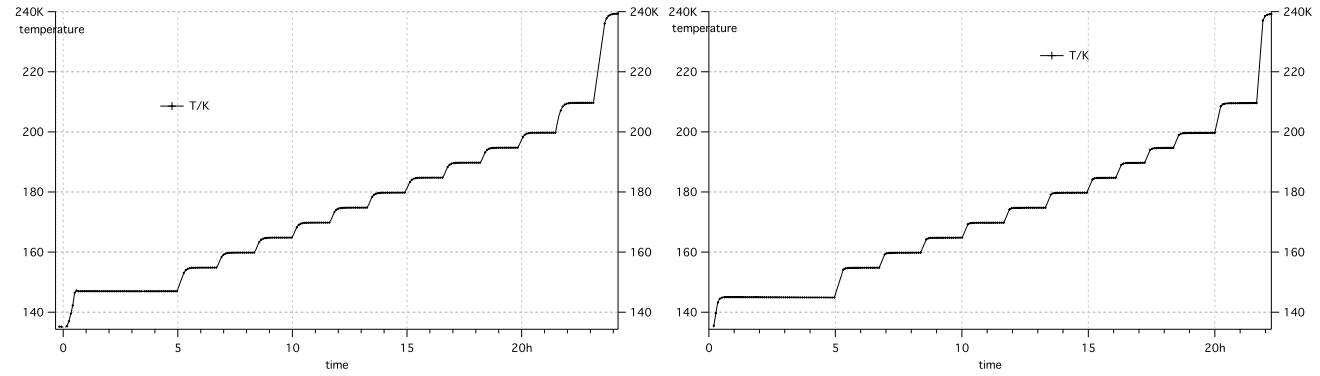

Figure 1. Overview of the temperature dependence on time for the two measurement series starting from ice V (left) and ice IX (right) on the powder diffractometer D20.

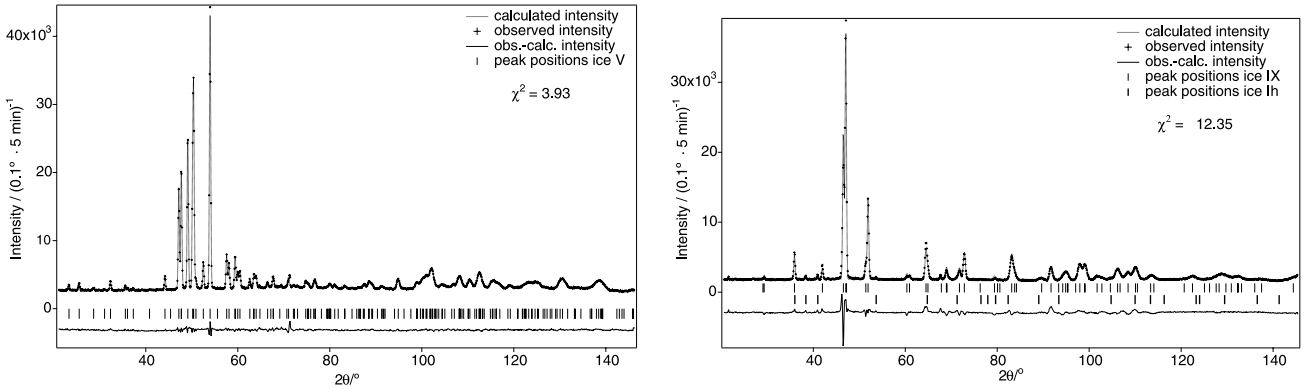

Figure 2. Rietveld fit of precursor ice V at 122 K (left), 0.3 h before the start of the experiment, and ice IX at 106 K (right), considered as the starting point of the experiment.

for a sufficiently long time at 145 or 147 K to allow for the complete relaxation of the precursor to ice Ic (about 4.5 h). The temperature was then increased to 155 K, kept at least 1.5 h, increased by 5 K, again kept at least 1.5 h, and so on up to 200 K, then 210 and 240 K as shown in figure 1.

2.3. Small angle neutron scattering

Additional small angle neutron scattering (SANS) experiments have been performed at the lowest momentum transfer SANS instrument D11 [38, 39] at ILL. The two precursor samples came from the same sample preparation and were subjected inside an *Orange Cryostat* to the same temperature programme as on D20. Data were recorded at a wavelength of $\lambda \approx 4.51$ Å during 5 min with a detector–sample distance of 10, 2.5 and 1.1 m, respectively. A 5 min transmission measurement at the longest distance was part of the measurement cycle as well. In total, a cycle of these four measurements of 5 min each took nearly 27 min, including the detector- , collimator- and attenuator-displacements. After the completed formation of ice Ic, in the case of the ice V relaxation at the end of the temperature step at 160 K, after 16 h, the programme was slightly changed: each temperature step (from 165 up to 200 K in steps of 5 K, plus 210 and 240 K) was covered by 6 of the described cycles (with shorter acquisition times of 2 min, respectively 150 s for the transmission measurement) plus one very low Q measurement of 120 s at the beginning, with a detector–sample distance of 36.7 m. Due to the long displacement, in total 20 min were spent on each of these very low Q measurements. Every temperature step, including the warming ramp took in total 1 h and 50 min.

3. Results

3.1. Precursors

We performed a sequential least-squares fit to the powder diffraction series starting from ice IX and from ice V. The precursor phases ice IX and ice V were refined from the initial untransformed powder patterns with the Rietveld-software *FullProf* [40]. The structure of ice V refined properly with complete proton-disorder, based on the structural data as published by Kamb *et al* [41], see figure 2, and also the structure of ice IX after Rabideau *et al* [42] fit the data relatively well, see figure 2. A fully proton-disordered structural model corresponding to ice III [43] delivers intensity ratios not in accordance with the diffraction pattern observed. Knowing that (1) full proton order is difficult to achieve [44] and that (2) ice III exhibits partial ordering [45] an attempt was made to refine the two order parameters as defined in [45] resulting in $\alpha_D \rightarrow 0$ and $\beta_D \rightarrow 0$. This corresponds to the fully ordered ice IX. It should be mentioned that *ab initio*

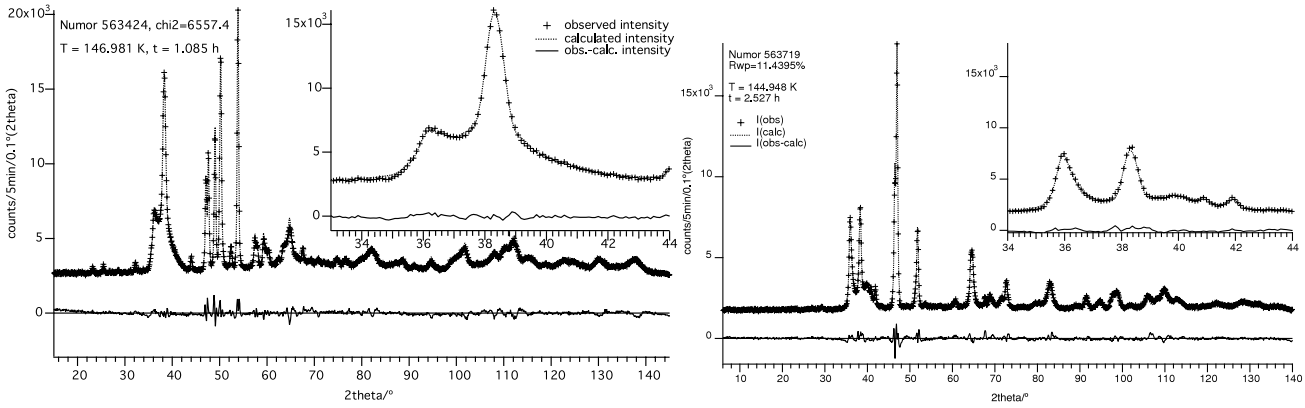

Figure 3. Diffraction pattern and fit of ice Ic and ice V at 147 K after 1.1 h with 47% of precursor still present (left) and of ice Ic and ice IX at 145 K after 2.5 h with 49% of precursor still present (right).

calculations [46] indicate a ground state with $\alpha, \beta \to 0$ which is energetically not much lower than the state in which $\alpha, \beta \to 1$, the latter even previously suggested to be the lowest energy conformation [47].

Weak remaining diffraction peaks were identified to originate from a small amount of ice Ih (2%). Argon clathrate hydrate, which may have formed in the preparation was also introduced but not confirmed in the refinement.

The precursor phases were fitted together with the ice Ic model as a second, stacking fault free phase, implementing the Rietveld method in our refinement routine. We refined the respective scale factors, an isotropic overall Debye–Waller factor B_{O} for oxygen and another one, B_{D}, for hydrogen, respectively deuterium, the lattice parameters a, b, c and β for ice V (monoclinic), respectively a and c for ice IX (tetragonal), as well as an isotropic particle size-broadening parameter a_{00}, which turned out to change considerably at the onset of formation of ice Ic (the particle size doubles within the first 10 min of formation of ice Ic from ice V). Atom position parameters were taken from the initial refinement of the pure phase and were kept fixed. The contamination with ice Ih in the ice IX precursor was added to the computed powder patterns of that series. The refined parameters were a scale factor, Debye–Waller factors B_{O} and B_{D}, lattice parameters a and c, anisotropic size-broadening parameters a_{00} and a_{20}, the relative position of oxygen d in the direction of the fractional co-ordinate z and the relative position g of hydrogen on the connection line between neighbouring oxygen positions as used in equation (6) of [1] for the description of ice Ic. In the same way as for ice Ic, experimentally determined peak-shapes were used for all phases, as described in [1].

3.2. Formation of ice Ic

The transformation of the recovered high-pressure phase into ice Ic was studied at constant temperature. To fit the observed powder patterns, a scale factor, four coefficients of a cubic background polynomial, an overall isotropic Debye–Waller factor $B^{\mathrm{iso}}_{\mathrm{overall}}$, the anisotropic size-broadening parameter in the basal plane a_{00}, the lattice parameters of the primitive trigonal cell a and c, the fractional co-ordinate d of oxygen and a co-ordinate g of the position of hydrogen on the connection line between two oxygen atoms have been refined. Finally, of course, we refine N_c and the probabilities α, β, γ and δ as defined in [1]. Constraints have been applied, e.g., $N_c > 2$, $0 < \alpha < 1$, $0 < \beta < 1$, $0 < \gamma < 1$, $0 < \delta < 1$, to avoid divergence in cases where the refinement is less stable, i.e., if only a small proportion of ice Ic is present at the beginning of the relaxation of the high-pressure phase. In these cases, some parameters were kept fixed, as far as necessary.

In the following, time is given in hours from the (arbitrarily defined) beginning of either series of sequential data recording. In both cases, the 147 K stage for ice V and the 145 K stage for ice IX were reached after 0.5 h, after heating up from liquid nitrogen temperature.

The fit of the series of patterns starting from ice V went smoothly, whilst the data quality of the series of patterns starting from ice IX was somewhat lower due to a smaller amount of sample investigated. Moreover, also the quality of fit was lower, most likely reflecting the fact that the ice Ic phase is not sharply peaked enough around one set of probabilities α, β, γ and δ and one number of layers N_c. Instead, either a mixture of different ice Ic phases or a broader distribution of a particular shape (width and skewness) around the mean characterization needs to be refined. The former is theoretically possible with the model as it is implemented, only the computing time becomes a problem, the latter is an approach to be implemented in a future version for the refinement programme.

Some stages of the relaxation of ice V and of ice IX are shown in figures 3 and 4, respectively 3 and 5. At the onset of ice Ic-formation, the probabilities α, β, γ and δ are not very meaningful, therefore, these probabilities are only shown for ice Ic close to the end of the relaxation (figures 4, respectively 5).

3.3. Metastability of ice Ic

After its formation the evolution of ice Ic was followed by ramping up the temperature. Traces of ice IX are still present up to 160 K. Then, up to the stage of 185 K including, ice Ic is the only present phase, until the onset of ice Ih

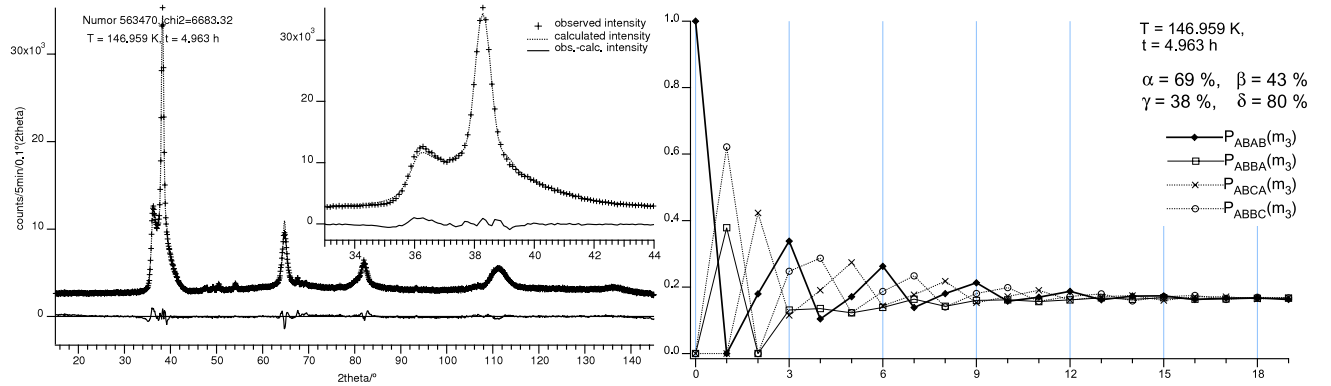

Figure 4. Diffraction pattern and fit of ice Ic from ice V at the end of the 147 K stage after 5 h (left). The unfitted peak and diffuse intensity at $2\theta \approx 68°$ is due to vanadium from the cryostat's calorimeter. The small peaks around $2\theta \approx 50°$ are due to remaining ice V (less than 0.5%). Right side: corresponding pair correlation probabilities in ice Ic at these conditions.

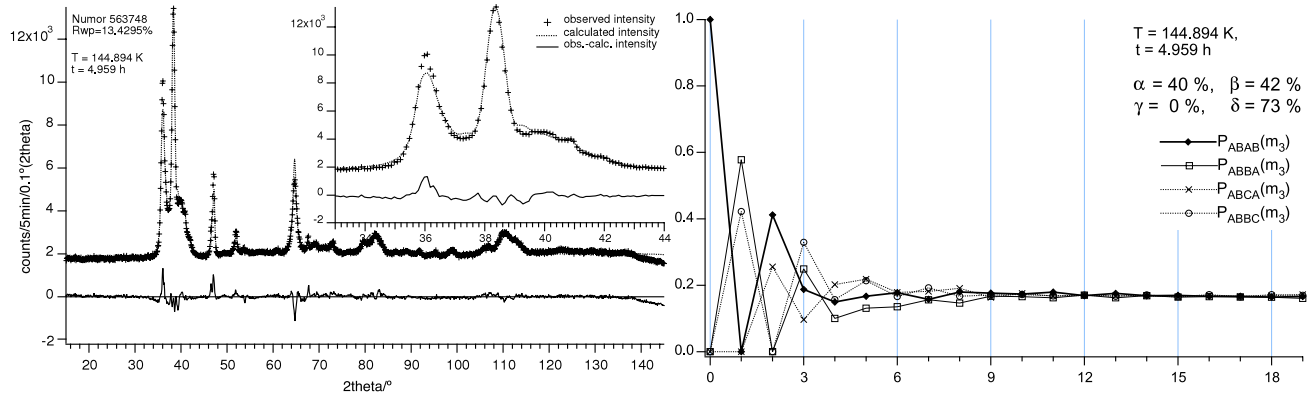

Figure 5. Diffraction pattern and fit of ice Ic from ice IX at the end of the 145 K stage after 5 h. Ice IX is still 10% present. Beside pair correlation probabilities in ice Ic at these conditions.

(either as individual crystallites or as part of modified stacking sequences, see section 3.4) formation at 190 K. Only the crystallite size changes slowly and regularly with time and temperature, while the characteristics of the stacking disorder, expressed by α, β, γ and δ, and, alternatively, by the seed probabilities w_{HK}, w_{HH} and w_{KK} or simply by the probability of hexagonal or cubic stacking do not change significantly.

Without a significant amount of a minority phase present, ice Ic from ice V refines properly, whereas ice Ic from ice IX shows some inconsistencies as already mentioned in 3.2. Both, the initially formed ice Ic obtained from ice V and the finally formed ice Ih can be described with a characteristic set of probabilities α, β, γ and δ and N_c. The model was used to fit all data sets from the formation of ice Ic up to the onset of transformation of ice Ic into ice Ih at about 185 K. For these states of ice Ic we show the pair correlation probabilities $P_{AB\cdot AB}(m_3)$, $P_{AB\cdot BA}(m_3)$, $P_{AB\cdot BC}(m_3)$ and $P_{AB\cdot CA}(m_3)$ as well (figures 6–8).

Particularly important is the evolution of the four probabilities α, β, γ and δ (figure 9), the evolution of the proportion of hexagonal and cubic sequences as well as pairs of them (figure 10), as resulting from these probabilities after [1]. Ice Ic from ice V has about the same set of probabilities over 12 h, with β and γ slightly below 40%, whereas δ is around 80% (thus the probability of having clusters of three cubic sequences or more is high) and α around 70% (thus two hexagonal sequences are normally enclosed in cubic sequences—which is the definition of a deformation fault in cubic packing). Cubic sequences are present in ice Ic from ice V up to about 60%.

The fact that pairs of two hexagonal sequences (w_{HH}) appear as often as each one of both probabilities of having pairs of cubic and hexagonal stacking sequences in either order (w_{HK} and w_{KH}), up to about 20% is compatible with hexagonal sequences always appearing in isolated pairs (deformation faults). Other arrangements would also be compatible with the obtained stacking pair-occurrence probabilities, yet the likelihood of deformation faults is always higher than for growth faults: with $\gamma = 37\%$, the situation illustrated in figure 6, 37% of hexagonal sequences following cubic ones are growth faults (followed by a cubic sequence). With $\alpha = 62\%$, $0.62(1-0.37) = 39\%$ of hexagonal sequences following cubic ones are part of isolated deformation faults, 15% are part of blocks of three, 6% of blocks of four, 2% of blocks of five and 1% of blocks of six or more hexagonal sequences. The idealized case of faults occurring exclusively as growth/twin or deformation faults, i.e. as single or double hexagonal sequences in a cubic lattice, is described

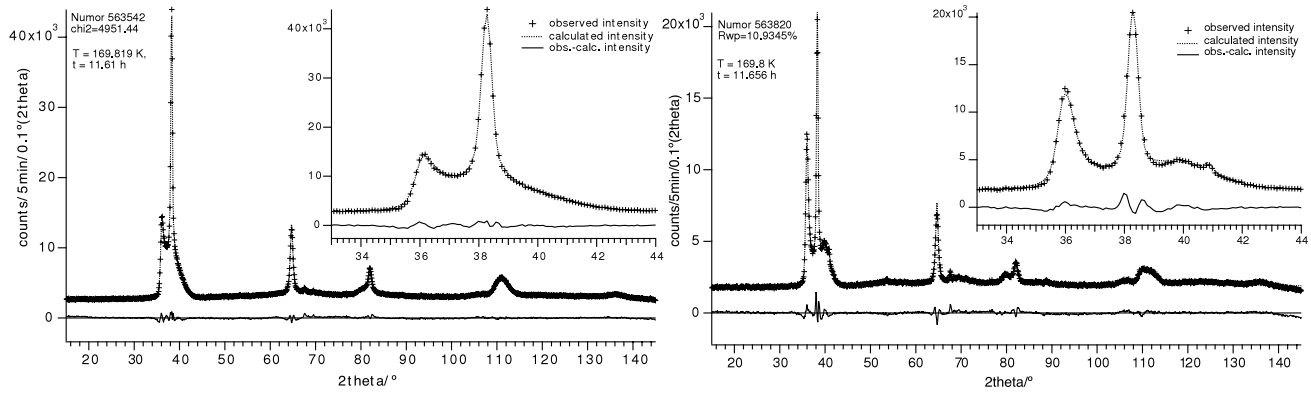

Figure 6. Diffraction pattern and fit of ice Ic from ice V after 11.6 h (left) and ice IX after 11.7 h (right) at the end of the 170 K stage. The amount of ice Ih is not significant for the sample formed from ice V and must be less then 0.5%. The sample formed from ice IX shows a 5% contamination with ice Ih which is due to the formation and recovery process of ice IX with no indication of further increase at this point. The stacking probabilities are $\alpha = 62\%$, $\beta = 38\%$, $\gamma = 37\%$ and $\delta = 78\%$, respectively $\alpha = 29\%$, $\beta = 55\%$, $\gamma = 5\%$ and $\delta = 66\%$.

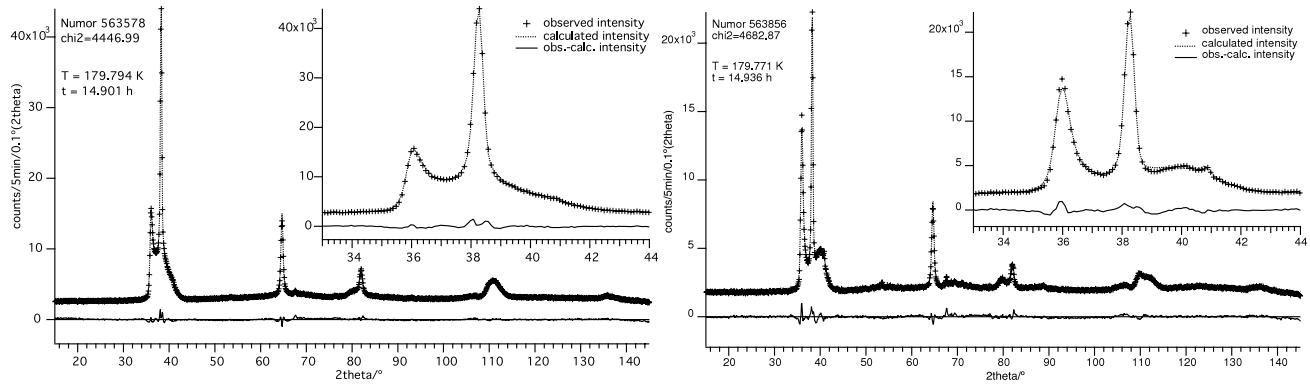

Figure 7. Diffraction pattern and fit of ice Ic from ice V (left) and ice IX (right) at the end of the 180 K stage after 14.9 h. The amount of ice Ih could represent possibly 1.3% of the total amount of ice, respectively 5%. The stacking probabilities are $\alpha = 55\%$, $\beta = 43\%$, $\gamma = 38\%$ and $\delta = 76\%$, respectively $\alpha = 30\%$, $\beta = 49\%$, $\gamma = 3\%$ and $\delta = 65\%$.

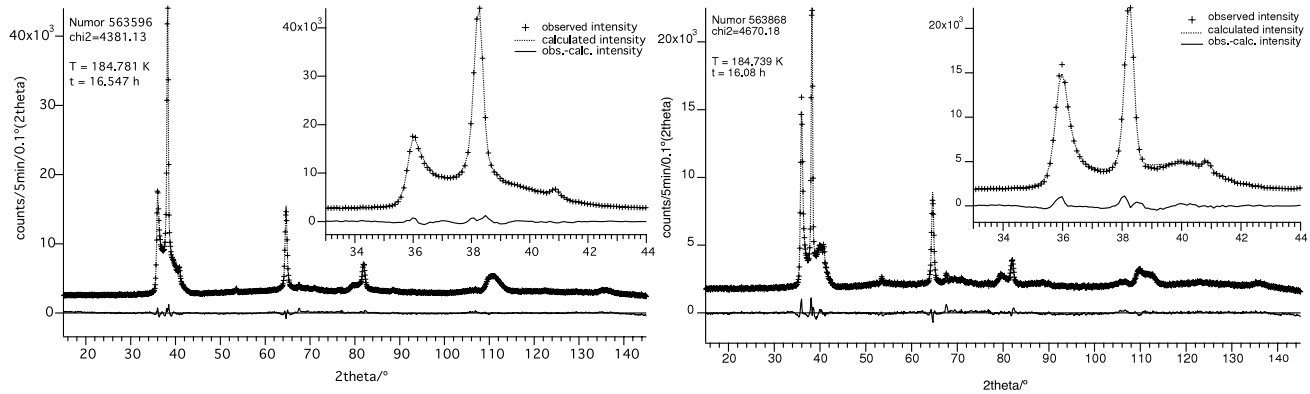

Figure 8. Diffraction pattern and fit of ice Ic from ice V after 16.5 h (left) and ice IX after 16.1 h (right) at the end of the 185 K stage. The amount of ice Ih represents a no longer negligible 3.5% of the total amount of ice, respectively 5%. The stacking probabilities are $\alpha = 55\%$, $\beta = 39\%$, $\gamma = 36\%$ and $\delta = 76\%$, respectively $\alpha = 28\%$, $\beta = 54\%$, $\gamma = 9\%$ and $\delta = 61\%$.

by equation (7) in section 3.3 of [1]. In that case, γ gives the proportion of growth faults, and a value below 50% would thus stand for a majority of deformation faults.

In parallel with the transformation to ice Ih, with an onset during the 180 K stage, before it is all α, which decreases first slowly, at 190 K dramatically, leading mainly to an important increase of clusters of more than two hexagonal sequences at the expense of cubic sequences. At first, below 190 K, this growth of hexagonal domains is not accompanied by a decrease of the number of interfaces between hexagonal and cubic domains (w_{HK}), which means that these domains grow from existing pairs of hexagonal sequences into cubic domains

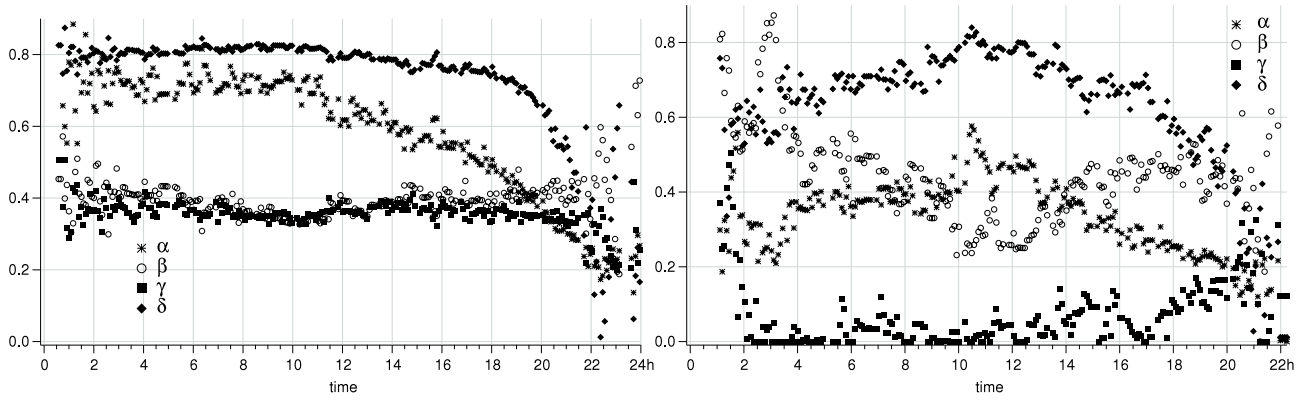

Figure 9. Evolution of α, β, γ and δ over time for ice Ic from ice V (left) and ice IX (right).

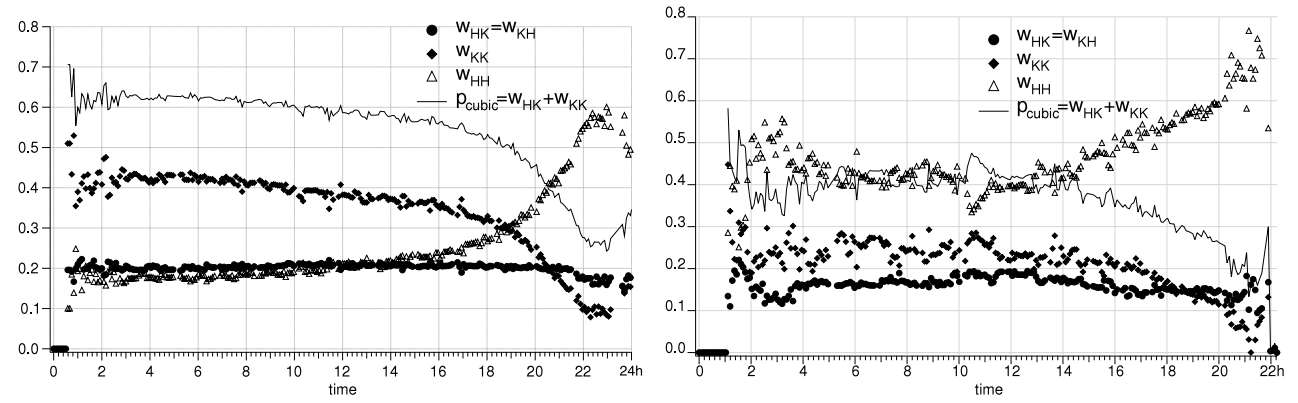

Figure 10. Evolution of the proportion of cubic sequences over time ($w_{HK} + w_{KK}$), of the probability to find pairs of similar stacking (w_{KK} and w_{HH}) and interfaces between different stacking types (w_{HH}) for ice Ic from ice V (left) and ice IX (right).

and do not form spontaneously inside clusters of cubic stacking sequences.

Ice from ice IX (figures 9 and 10) looks rather different: γ is zero or close to zero, which means that single hexagonal sequences are forbidden, α is much lower and varies between 20% and 40%. In contrast to ice Ic from ice V it is slowly increasing up to 175 K. Its low value compared to ice Ic from ice V means a higher number of clusters of more than two hexagonal sequences. δ is, as in the case of ice Ic from ice V, higher than α and shows a similar variation over time and temperature between 60 and 80%, whereas β decreases over time from 60% to 30%. As a result, the concentration of cubic sequences is not constant, but reaches a broad maximum at 175 K of about 42%, starting at about 25% during formation at 145 K. As expected, it decreases during the transformation to ice Ih. w_{HH} has more than 40% at any time, considerably higher than w_{HK}, which, again, means that clusters of more than two hexagonal sequences are frequent. Ice Ic is slightly less rich in interfaces between the cubic and the hexagonal stacking rule than ice Ic from ice V, with w_{HK} varying around 15%.

The evolution of the crystallite size parallel to $\vec{c}$, $D_{00l} = N_c \cdot c$, and perpendicular to $\vec{c}$, $D_{hk0} = 2/3 \cdot a_{00}$, following [1], is shown in figure 11. It is remarkable, in the case of ice Ic from ice V, that in the region of metastability of ice Ic, the crystallites have the same extension in both crystallographic main directions. They are isometric, neither platelet, nor needle shaped. The crystals grow continuously, once formed at 147 K after 4 h with a particle size of 250 Å, nearly linear with time and temperature up to the end of the 190 K stage after 18 h to 700 Å. During the following transformation to ice Ih, the particle size of the remaining ice Ic continues to grow in the direction of $\vec{c}$. The behaviour of ice Ic formed from ice IX is more or less identical, with a particle size of 200 Å at the end of the formation after 5 h, the original particles are slightly smaller but grow to similar sizes at 190 K.

3.4. Transformation to ice Ih

We shall have a closer look at the two-phase region Ih/Ic. During the slow transformation of ice Ic to Ih, there is clear evidence not of a gradual annealing of the existing ice Ic crystals, but instead of a formation of relatively pure (in terms of stacking fault concentration) ice Ih at the expense of ice Ic. After the onset of transformation to Ih, the refinements of patterns become gradually worse, in terms of the χ^2 of the least-squares method. This can be remedied by refining the data with a mixture of two phases, one originating from the previously refined ice Ic and the other from the final ice Ih. It would probably be more physical to allow for long hexagonal sequences in our stacking model. However, if extended hexagonal sequences are handled together with the initial ice Ic

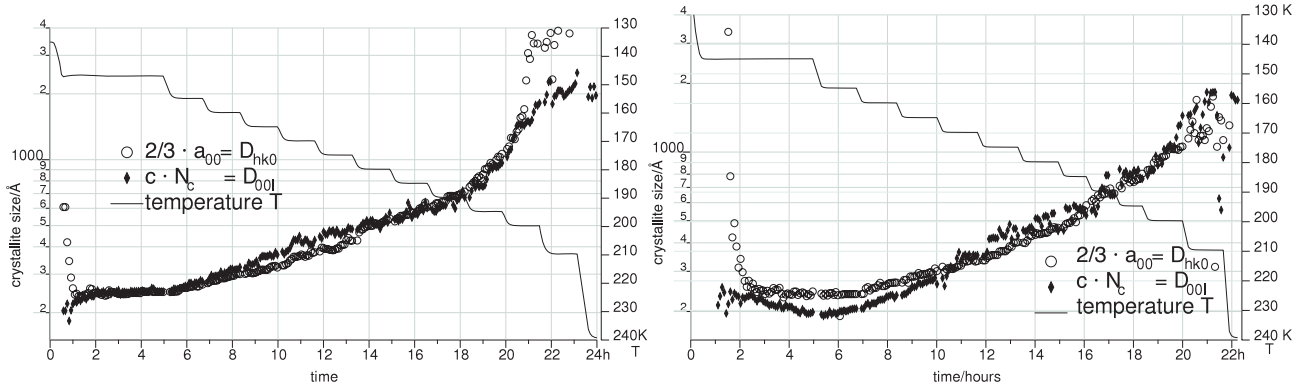

Figure 11. Evolution with time of the crystal size in the c-direction, D_{00l}, proportional to the number of layers N_c (with ≈ 3.67 Å per layer), and D_{hk0}, the size perpendicular to the stacking direction $\vec{c}$, for ice Ic from ice V (left) and ice IX (right). For orientation, the temperature (with reverse axis, for clarity) dependence on time is plotted as a solid line.

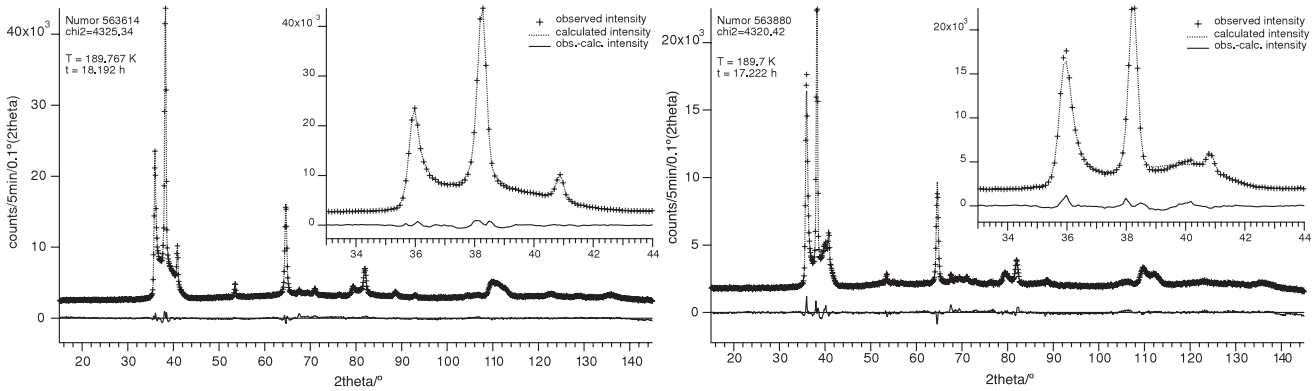

Figure 12. Diffraction pattern and fit of ice Ic from ice V after 18.2 h (left) and ice IX after 17.2 h (right) at the end of the 190 K stage. The amount of ice Ih represents 11% of the total amount of ice, respectively 8%. The stacking probabilities are $\alpha = 47\%$, $\beta = 41\%$, $\gamma = 37\%$ and $\delta = 73\%$, respectively $\alpha = 28\%$, $\beta = 49\%$, $\gamma = 6\%$ and $\delta = 64\%$.

stacking in our model, the computing time becomes enormous (up to one day per pattern), due to the large size of the ice Ih sequences, thus a large value of N_c. It is far more convenient to refine a mixture of ice Ic, modelled as described here, and a conventionally described ice Ih phase, which has a few parameters (scale factor, lattice constants, fractional coordinate z of the oxygen position, the relative position g of the hydrogen positions on the link between two oxygen positions and a parameter for anisotropic peak broadening). This second phase can be handled by the conventional Rietveld method, which is much faster than the stacking fault model. Once the second phase is introduced, the further refinement in the region of coexistence delivers fits of similar quality in terms of χ^2 as in the region of pure ice Ic (see, e.g., figures 12 and 13).

The evolution of the scale factors will not easily allow one to obtain precise information about the transformation kinetics and thus the activation energies with the Arrhenius equation, as the remaining ice Ic as a result of the refinement shows increasing characteristics of ice Ih with $\alpha, \beta, \gamma, \delta \rightarrow 0$ (see figures 9 and 10). The scale factor of ice Ic can thus not simply be taken as the fraction of initial material in an Avrami approach [48–50].

The finally formed ice Ih can be as easily described with a characteristic set of probabilities and N_c. However, as N_c becomes very large (>800), the computing becomes very slow, for a result by no means different from a conventional Rietveld refinement, as the finally formed ice Ih is perfectly hexagonal without stacking faults and forms large crystallites. In figures 14 and 15, at the end of the 210 K stage, there is still a tiny amount of ice Ic present, as obvious from the fact that the second peak 200 of ice Ih shows a higher amplitude than the third one 101; in pure ice Ih the ratio is the reverse. Beneath the 200 peak, the 111 peak of ice Ic (with its 'traditional' cubic setting—its indexing in the model presented here would be 001 instead) adds intensity to the 200 peak of ice Ih and suggests a stacking-faulted ice Ih. This suggests some remaining stacking faults somewhere in the sample largely dominated by purely hexagonal stacking sequences but with some remains of the faulty sequences of ice Ic.

At 240 K, finally, the pattern (figure 16) can be perfectly fitted with pure ice Ih without any faults as observed before by Kuhs *et al* [4].

3.5. Correlation with SANS observation

SANS data have been reduced by means of standard software [51–53]. Selected data sets taken at sample–detector distances of 1.1, 2.5 and 10 m are reported in figure 17.

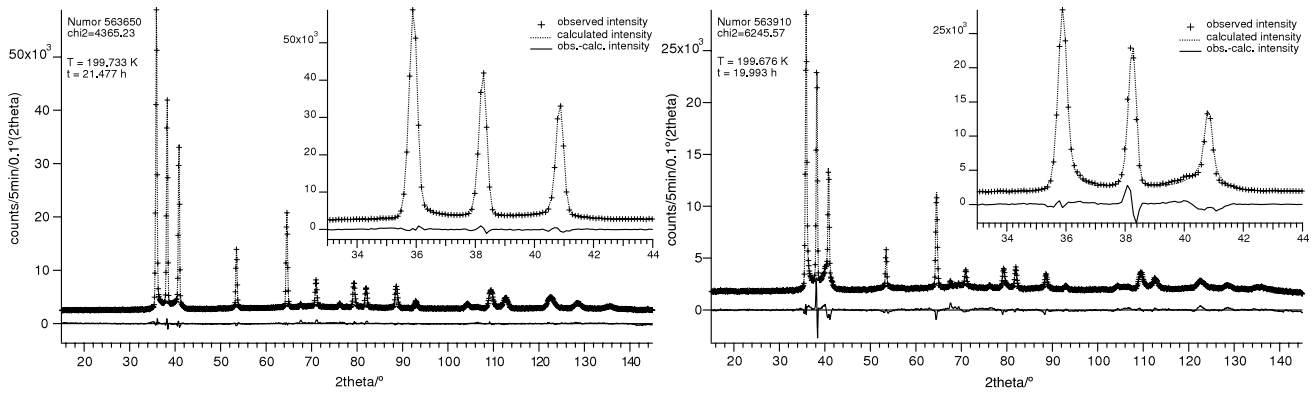

Figure 13. Diffraction pattern and fit of ice Ic from ice V after 21.5 h (left) and ice IX after 20 h (right) at the end of the 200 K stage. The amount of ice Ih represents 63% of the total amount of ice, respectively 50%. The stacking probabilities are $\alpha = 28\%$, $\beta = 44\%$, $\gamma = 35\%$ and $\delta = 42\%$, respectively $\alpha = 12\%$, $\beta = 48\%$, $\gamma = 15\%$ and $\delta = 41\%$.

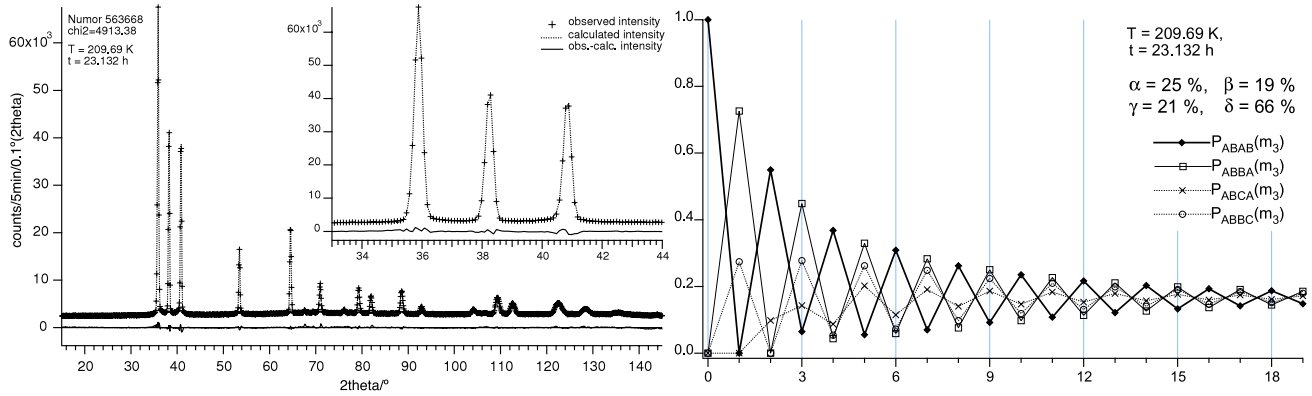

Figure 14. Diffraction pattern and fit of ice Ic from ice V at the end of the 210 K stage after 23.1 h (left) and pair correlation probabilities in ice Ic at these conditions (right). The amount of ice Ih represents 75% of the total amount of ice.

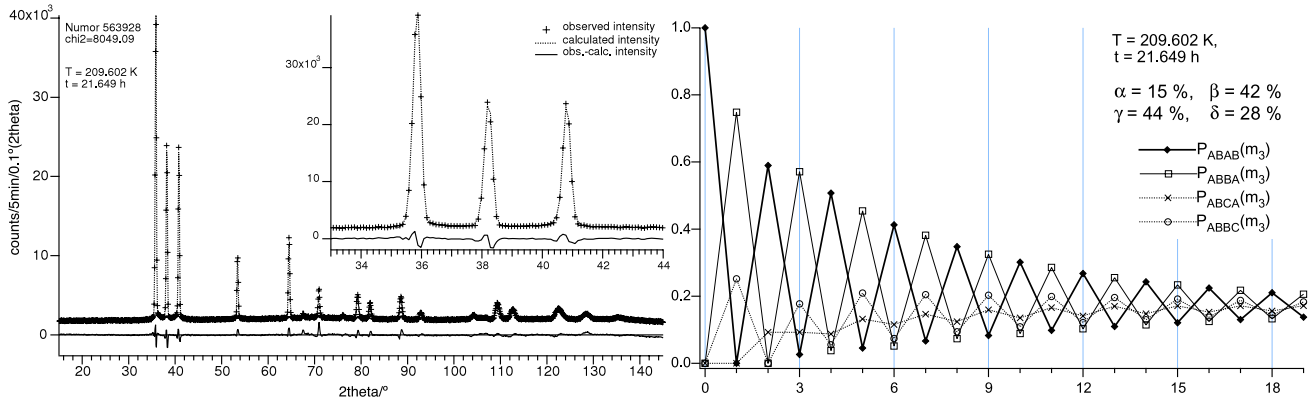

Figure 15. Diffraction pattern and fit of ice Ic from ice IX at the end of the 210 K stage after 21.7 h (left) and pair correlation probabilities in ice Ic at these conditions (right). The amount of ice Ih represents 82% of the total amount of ice.

Over the whole Q-range covered, the small angle scattering of the observed ice phases in all states of relaxation and transformation at different temperatures follows approximately a Q^{-4} behaviour. The flat background observed at high momentum transfers Q is due to the incoherent scattering of the sample.

The pronounced power-law dependence of the observed intensity Q^{-4} is the so-called Porod-limit scattering. It is the final slope of a SANS form factor that appears due to a boundary between two phases in a sample and depends only on the scattering contrast and the interface area, but not on the shape of the structures or particles present in the sample [54, 55]. At low Q, our data do not cover the range necessary to observe a Guinier-limit scattering. The Porod-limit scattering intensities I_p were determined to be between $2.4003(2) \times 10^{-15}$ and $3.489(5) \times 10^{-14}$ Å^{-1} for the ice V

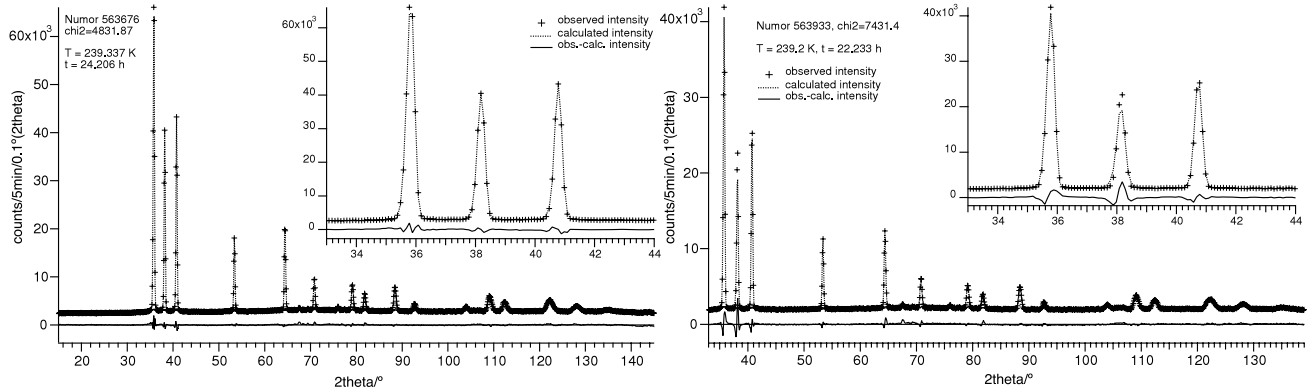

Figure 16. Diffraction pattern and fit of ice Ih from ice V (left) and ice IX (right) at the end of the 240 K stage after 24.2 h, respectively 22.2 h.

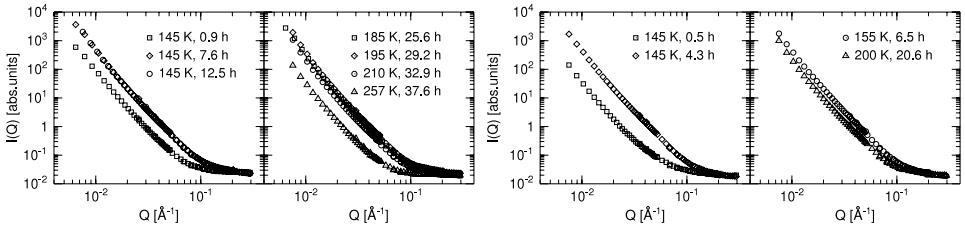

Figure 17. Double logarithmic plot of radially integrated scattering intensity versus Q for ice Ic from ice V (left) and ice IX (right) for some measurements during the Ic-formation at 145 K (left) and the transformation to Ih.

relaxation experiment and between 2.8853(5) $\times$ 10^{-15} and 3.354(2) $\times$ 10^{-14} Å^{-1} for the ice IX relaxation experiment. These values were obtained with a fitted linear background from incoherent scattering, which gives the highest confidence. However, even when using the measured background from incoherent scattering instead, one obtains values, which vary by 2% at most from the given ones. Under the assumption of spherical particles with a surface $4\pi r^2$ we obtain the particle radii as $r = 2\pi(\Delta\rho)^2/3I_\mathrm{p}$. Assuming only interfaces between grains of ice and vacuum, the contrast of scattering intensities becomes identical to the scattering density of ice $\Delta\rho = \sum b_i/V$, which is about 5.4 $\times$ 10^{-6} Å^{-2} for ice Ic and Ih, 7.1 $\times$ 10^{-6} Å^{-2} for ice V and 6.7 $\times$ 10^{-6} Å^{-2} for ice IX. Under this assumption, we obtain grain diameters ranging from 2920 (ice Ic at 185 K) to 24500 Å (ice Ih at 257 K) in the ice V relaxation experiment and from 4090 (ice Ic at 200 K) to 34300 Å (ice IX at 145 K) in the ice IX relaxation experiment, virtually independent on the correction of the incoherent signal. These values exceed by an order of magnitude what we would expect from the result of the powder diffraction investigation. Note however, that they are in reasonable agreement with the diffraction observation, as we must consider not only ice–vacuum but also ice–ice interfaces, the latter showing a contrast reduced by one order of magnitude when compared with the one of the ice–vacuum interface. To reconcile the findings of particle sizes obtained from the Scherrer formula with the SANS results, interfaces of lower contrast must exist, but for a quantification of the type and frequency of such interfaces, further experiments need to be performed.

It is remarkable, that the integrated low-Q signal—proportional to I_p and grain boundary contrast and inversely proportional to grain size—increases massively during the relaxation of ice V to ice Ic, due to the small particle size of ice Ic, as expected from the result of the powder diffraction data modelling. This is visible from figure 18. The intensity maximum for the case of ice IX transforming into ice Ic is reached between 150 and 155 K, i.e., later than in the ice V case. It is interesting to note that the transformation ice IX still proceeds at these temperatures and is completed only at about 160 K as evidenced from powder diffraction. In the region of metastability of ice Ic, the intensity of this signal decreases slightly from 150 to 185 K, due to the annealing of ice Ic to slightly larger crystallites, again, as obtained from the evaluation of the powder diffraction data. Between 185 and 195 K the signal increases again, and between 195 and 200 K reaches a level close to the maximum at 145 K. The onset of this rise corresponds to the appearance of ice Ih at 185 K (figure 8). This observation demonstrates an astonishingly high sensitivity of the SANS signal: the density of ice Ic at these temperatures is 99.9% of the one of ice Ih. Despite this fact we are apparently able to observe the formation of ice Ih. The fact that the ice Ic–ice Ic crystallites clearly with no scattering contrast also contribute to the SANS signal as evidenced in the intermediate temperature range, suggest that these interfaces contain voids enhancing the contrast. Similarly, the ice Ih–ice Ic interfaces may contain voids and the increase of signal observed upon ice Ih-formation may be due to the formation of new ice Ih crystallites within the old interface increasing the total interface area. Yet, other scenarios are conceivable and

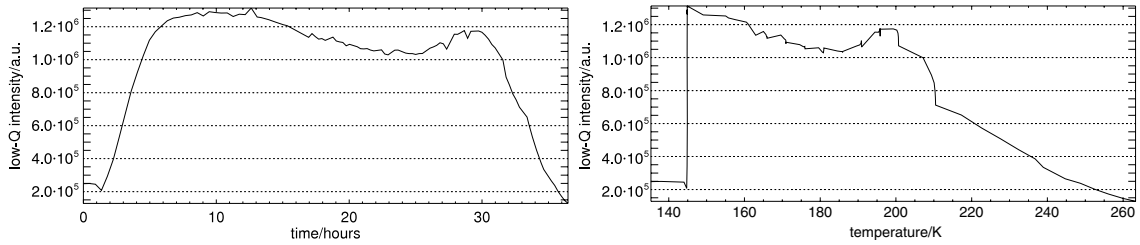

Figure 18. Total integrated scattered intensity during ice V relaxation and ice Ic transformation at low Q configuration (detector–sample distance 10 m) as a function of time (left) and temperature (right).

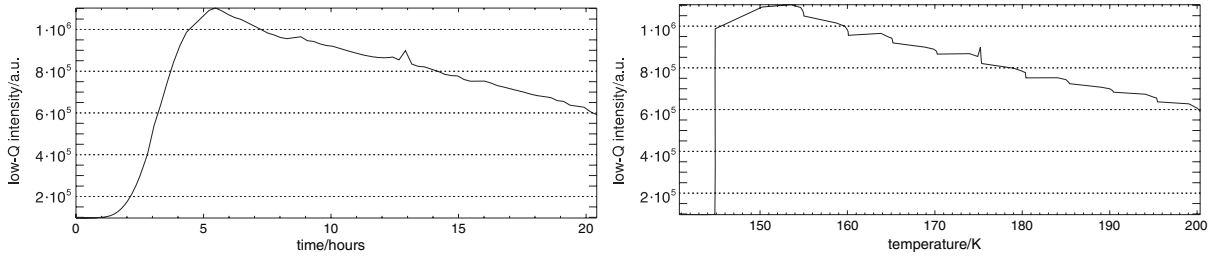

Figure 19. Total integrated scattered intensity during ice IX relaxation and ice Ic transformation at low Q configuration (detector–sample distance 10 m) as a function of time (left) and temperature (right).

further work is needed to settle the issue. The signal starts to decrease linearly with time at 200 K, when ice Ih becomes the major phase. Again, this is in perfect agreement with the result obtained from the modelling of the powder diffraction data: ice Ih forms huge crystallites, compared to ice Ic.

The relaxation of ice IX and subsequent transformation to ice Ih is shown in the figure 19. The same dramatic rise in signal on formation of ice Ic appears, but afterwards there is a continuous decrease (linear with time) in the signal as the ice Ic crystallites slowly grow. There is no increase at the onset of transformation to ice Ih at 185 K. The expected steep decrease above 200 K has not been observed here, as the temperature programme was stopped before.

4. Discussion

It has already been found earlier, e.g. [56], that different precursors produce a characteristic pattern of ice Ic, which should result in a specific probability of stacking polytypes in our model. Indeed, ice Ic from ice V and from ice IX are quite different in this respect as shown in figure 9. The differences between ice Ic of different origin are also clearly visible in figures 4 and 5 with pair correlation probabilities reaching further in the case of ice Ic formed from ice V. Moreover, the corresponding probability distribution changes little with increasing temperature suggesting that the original pattern is largely preserved up to the point where the transformation into ice Ih sets in. Our T-dependent analysis suggests that the main changes in this region relate to the crystallite size. Our SANS results confirm this increase of particle size as evidenced by the decrease of scattering signal.

It is worth noting, that the onset of the transformation into ice Ih is accompanied by an increase in the total SANS intensity for the case of ice Ic formed from ice V but not for ice Ic formed from ice IX. This may suggest that new small crystallites of ice Ih are formed in the former case leading to additional interfaces. The lower percentage of hexagonal stacking in ice Ic formed from ice V [1] may render difficult stacking rearrangements to form ice Ih sequences, resulting in a need for nucleation of new hexagonal crystallites in contrast to the ice IX case, for which internal stacking rearrangements may allow the formation of extended ice Ih sequences.

The observations presented here are in good agreement with a number of electron-microscopic studies as well as with earlier diffraction results obtained from peak broadening via the Scherrer formula. Most electron-microscopic studies of cubic ice were performed on material formed by *in situ* vapour deposition either directly or via a transformation from deposited amorphous ice. Therefore, we cannot be sure that these results are directly comparable. Nevertheless, it appears that good agreement exists: Kumai [24] finds crystallite sizes between 100 and 500 Å increasing with increasing temperature. Vertsner and Zhdanov [57] found seemingly anisotropic ice Ic crystallites of 300 to 600 Å in width and 100 Å parallel to the substrate when formed from vapour at −130 °C. Meryman [58] has conducted an electron-microscopic experiment of the annealing of ice Ic in the temperature range from −96 to −70 °C; the particles increased from below 100 nm to almost micron-size in this temperature range. At −120 °C distinctly larger isometric crystallites of about 300 nm were found by [59], again in a formation from water vapour. The crystallite size of about 250 Å found for ice Ic as formed from recovered high-pressure ices falls in the lower range of these observations. We do not know, however, whether systematic differences in size exist between cubic ices of different origin or whether isothermal annealing leads to the observed size variation. What is safely established from our work is a temperature-driven increase of crystallite size

for the cubic ices studied here. These findings corroborate earlier diffraction work: Londono [60] reported sizes from 215 Å at 100 K and 384 Å at 176 K as obtained from the peak broadening of high-resolution neutron diffraction data [3] in good agreement with our far more detailed analysis.

It is interesting to note that the crystallite sizes correspond to the size of mesopores, in which ice Ic can be kept up to the ice melting point after formation from freezing liquid water. Moreover, the calculated patterns obtained for different values of N_c correspond to the ones shown by Morishige and Uematsu [18]. Their suggestion that sufficiently small Ic crystals are stable compared to ice Ih, if there is no possibility to grow larger and eventually convert into ice Ih crystals, is compatible with our results. Moreover, the similarity of the observed powder patterns suggests that stacking-faulty ice Ic is the generally favoured product whenever particles remain small. This also suggests that the critical nucleus of ice Ic (with or without stacking faults) is energetically more favourable than the purely hexagonal form, as has been suggested for snow crystallization at large undercooling [61]. These authors provide experimental evidence that a nascent snow crystal will turn upon further growth into a hexagonal crystal, possibly with a remaining cubic core. However, to what extent this growth process can be related to the annealing of ice Ic described here remains an open question.

5. Summary

Between the formation of first ice Ic crystallites from ice V at 147 K and the onset of ice Ih-formation at 190 K, 18 h later, the mean crystal size in the $\vec{c}$-direction grows from about 50 to 180 layers (180 to 660 Å). Perpendicular to this direction, the size triples as well over the same temperature range. During the transition from faulty ice Ic to clean ice Ih, there is a gradually changing frequency and pattern of hexagonal stacking sequences which from a certain point onwards can be described either as a stacking-faulty ice Ic with large purely hexagonal stacks or as a mixture of small crystallites of faulty ice Ic together with pure ice Ih.

6. Conclusion

The time-resolved aspect of our experiments is not only the basis for a better understanding of the kinetics of the formation and transformation of ice Ic, some aspects of which will be the focus of more detailed analysis work in the future, but also helped in a crucial way to establish a working general structural model. To work out such a general model without the consistency checks from gradually changing data would have been a difficult task. The consistent results of the complete data sets, evolving with time and temperature, makes us confident that the description of the stacking faults is physically meaningful, a confidence, which could hardly be gained from fitting isolated data sets.

7. Outlook

Now that a quantitative description of ice Ic is possible, the formation kinetics of ice Ic starting from different precursors and the transformation to ice Ih can be investigated in much greater detail, using the existing data, e.g., by applying an Avrami-analysis [48–50] to the advancing transformation based on the refined phase fractions. While we can safely state, that different parent phases lead to different cubic ices, we only know at present for ice IX and ice V which stacking sequence probabilities result. Other parent phases should be investigated or re-analysed. This may ultimately provide further insight into the molecular rearrangements taking place during the phase transformation into ice Ic. It is quite likely that Bjerrum L-defects [20] play a considerable role in this transformation as suggested by Devlin *et al* [21]. Bjerrum defect migration is considered as the dominant process for mechanical and dielectric relaxation [62] and also directly evidenced in deuteron spin alignment work on ice Ih [22]. Without reorientational degrees of freedom, topological changes in the solid state seem impossible and it is at temperatures of 140 to 150 K that these reorientations reach laboratory timescales as found in dielectric work [63]. It appears that the topology of the parent phase water structure determines which stacking in the resulting ice Ic will form, each of them characteristic for a given parent phase topology. We have evidence (from further experiments not discussed here) that transformation temperature and thus transformation speed is of minor importance, but not negligible, as concerns the observed diffraction pattern.

We also need to evaluate quantitatively the recorded SANS data in order to corroborate the estimates from the structural analysis, and to further elucidate the significant differences in the transition region towards ice Ih between the ice IX and the ice V form of ice Ic. The least-squares method does not guarantee obtaining the best possible model, i.e., the correct set of probabilities α, β, γ and δ. An optimization method, like simulated annealing should be invoked in order to get close to the best solution, which can further be refined with the least-squares method (see [1]).

The structure model needs several extensions: as discussed in section 3.2 we may consider a distribution (Gaussian in the simplest case) around the mean values for the parameters α, β, γ, δ, N_c and a_{00} instead of the currently mono-disperse model. The computer-grown crystals leading to a certain set of pair correlation probabilities may be easily constructed by more complex rules than the ones used here; based upon the probabilities α, β, γ and δ, higher interaction ranges than $s = 4$ can be tested. It remains open, however, if diffraction data can provide enough information to distinguish more complex situations properly.

Acknowledgments

The authors thank the ILL for allocated neutron beam time (28th to 31st May 2007) and technical support on the instruments D20 and D11 in the frame of the proposal 5-24-271. We are grateful to Eberhard Hensel and Andrzej Falenty from the Universität Göttingen for the technical support during the sample preparation and the Deutsche Forschungsgemeinschaft (DFG) for financial support via the grant Ku-920/11 in the framework of its programme 'Mars and Earth-like planets'.

References

[1] Hansen T C, Koza M M and Kuhs W F 2008 Formation and annealing of cubic ice: I modelling of stacking faults *J. Phys.: Condens. Matter* **20** 285104

[2] König H 1943 Eine kubische Eismodifikation *Z. Kristallogr.* **105** 279–86

[3] Kuhs W F, Londono D, Mayer E, Hallbrucker A and Finney J L 1989 Neutron powder diffraction studies on the formation and stability of ice ic *Z. Kristallogr.* **186** 174–5

[4] Kuhs W F, Genov G, Staykova D K and Hansen T 2004 Ice perfection and onset of anomalous preservation of gas hydrates *Phys. Chem. Chem. Phys.* **6** 4917–20

[5] Koza M M, Geil B, Schober H and Natali F 2005 Absence of molecular mobility on nanosecond timescales in amorphous ice phases *Phys. Chem. Chem. Phys.* **7** 1423–31

[6] Lisgarten N D and Blackman M 1956 Cubic form of ice *Nature* **178** 39–40

[7] Dowell L G and Rinfret A P 1960 Low-temperature forms of ice as studied by X-ray diffraction *Nature* **188** 1144–8

[8] Bertie J E and Jacobs S M 1977 Far-infrared absorption by ices Ih and Ic at 4.3 K and the powder diffraction pattern of ice Ic *J. Chem. Phys.* **67** 2445–8

[9] Klotz S, Besson J M, Hamel G, Nelmes R J, Loveday J S and Marshall W G 1999 Metastable ice VII at low temperature and ambient pressure *Nature* **398** 681–4

[10] Klug D D, Paul Handa Y, Tse J S and Whalley E 1989 Transformation of ice VII to amorphous ice by melting at low temperature *J. Chem. Phys.* **90** 2390–2

[11] Kobayashi T, Furukawa Y, Takahashi T and Uyeda H 1976 Cubic structure models at the junctions in polycrystalline snow crystals *J. Cryst. Growth* **35** 262–8

[12] Gassendi P 1629 Phenomenum rarum romae observatum 20 martij, et ejus causarum explicatio *Technical Report* Amstelodami. Henr. Guerard

[13] Riikonen M, Sillanpää M, Virta L, Sullivan D, Moilanen J and Luukkonen I 2000 Halo observations provide evidence of airborne cubic ice in the earth's atmosphere *Appl. Opt.* **39** 6080–5

[14] Murray B J, Knopf D A and Bertram A K 2005 The formation of cubic ice under conditions relevant to earth's atmosphere *Nature* **434** 202–5

[15] Murray B J and Bertram A K 2006 Formation and stability of cubic ice in water droplets *Phys. Chem. Chem. Phys.* **8** 186–92

[16] Murray B J and Bertram A K 2007 Laboratory studies of the formation of cubic ice in aqueous droplets *Physics and Chemistry of Ice* (*Special publication series, vol 311*) ed W F Kuhs (Cambridge: Royal Society of Chemistry) pp 417–26

[17] Murphy D M 2003 Dehydration in cold clouds is enhanced by a transition from cubic to hexagonal ice *Geophys. Res. Lett.* **30** 2230

[18] Morishige K and Uematsu H 2005 The proper structure of cubic ice confined in mesopores *J. Chem. Phys.* **122** 044711–4

[19] Sugisaki M, Suga H and Seki S 1968 Calorimetric study of glassy state. 4. heat capacities of glassy water and cubic ice *Bull. Chem. Soc. Japan* **41** 2591

[20] Bjerrum N 1951 Structure and properties of ice. 1. Position of the hydrogen atoms and the zero-point entropy. 2. Change in configuration and molecular turns. 3. Ionisation of ice and molecular turns produced by the ions—the proton jump conductivity of ice (and water) *Mat.-Fys. Medd. K. Dan. Vidensk. Selsk.* **27** 1

[21] Wooldridge P J, Richardson H H and Devlin J P 1987 Mobile Bjerrum defects—a criterion for ice-like crystal-growth *J. Chem. Phys.* **87** 4126–31

[22] Fujara F, Wefing S and Kuhs W F 1988 Direct observation of tetrahedral hydrogen jumps in ice lh *J. Chem. Phys.* **88** 6801–9

[23] Geil B, Kirschgen T M and Fujara F 2005 Mechanism of proton transport in hexagonal ice *Phys. Rev.* B **72** 014304

[24] Kumai M 1968 Hexagonal and cubic ice at low temperatures *J. Glaciol.* **7** 95–108

[25] Kuhs W F, Bliss D V and Finney J L 1987 High-resolution neutron powder diffraction study of ice I_c *J. Physique* C1 **48** 631–6

[26] Scherrer P 1918 *Nachr. Ges. Wiss. Gött.* **26** 98–100

[27] Koza M M, Hansen T, May R P and Schober H 2006 Link between the diversity, heterogeneity and kinetic properties of amorphous ice structures *J. Non-Cryst. Solids* **352** 4988–93

[28] Koza M M, May R P and Schober H 2007 On the heterogeneous character of water's amorphous polymorphism *J. Appl. Crystallogr.* **40** s517–21

[29] Kuhs W F, Hensel E and Bartels H 2005 Gas pressure cells for elastic and inelastic neutron scattering *J. Phys.: Condens. Matter* **17** S3009–15

[30] Bertie J E, Calvert L D and Whalley E 1963 Transformations of ice II, ice III, and ice V at atmospheric pressure *J. Chem. Phys.* **38** 840

[31] Gotthardt F 2001 *Dissertation* Georg-August-Universität Göttingen

[32] Garg A K 1988 High-pressure Raman-spectroscopic study of the ice Ih–ice IX-phase transition *Phys. Status Solidi* a **110** 467–80

[33] Ghormley J A 1968 Enthalpy changes and heat-capacity changes in the transformations from high-surface-area amorphous ice to stable hexagonal ice *J. Chem. Phys.* **48** 503–8

[34] Staykova D K, Kuhs W F, Salamatin A N and Hansen T 2003 Formation of porous gas hydrates from ice powders: diffraction experiments and multistage model *J. Phys. Chem.* B **107** 10299–311

[35] Kuhs W F and Hansen T C 2006 Time-resolved neutron diffraction studies with emphasis on water ices and gas hydrates *Neutron Scattering in Earth Sciences* (*Rev. Min. Geochem.* vol 63) ed Hans-Rudolf Wenk (Chantilly, VA: Mineralogical Society of America) pp 171–204

[36] Convert P, Hansen T, Oed A and Torregrossa J 1998 D20 high-flux two-axis neutron diffractometer *Physica* B **241–243** 195–7

[37] Hansen T C, Henry P F, Fischer H E, Torregrossa J and Convert P 2008 The D20 instrument at the ILL: a versatile high-intensity 2-axis neutron diffractometer *Meas. Sci. Technol.* **19** 034001

[38] Lindner P, May R P and Timmins P A 1992 Upgrading of the sans instrument D11 at the ILL *Physica* B **180/181** 967–72

[39] Lindner P and Schweins R 2008 Lowest momentum transfer and lowest background small-angle neutron scattering instrument D11 http://www.ill.eu/d11

[40] Rodriguez-Carvajal J 1993 Recent advances in magnetic structure determination by neutron powder diffraction *Physica* B **192** 55

[41] Kamb B, Prakash A and Knobler C 1967 Structure of ice V *Acta Crystallogr.* **22** 706–15

[42] Rabideau S W, Finch E D, Arnold G P and Bowman A L 1968 Neutron diffraction study of ice polymorphs. I. ice IX *J. Chem. Phys.* **49** 2514–9

[43] Kamb B and Prakash A 1968 Structure of ice III *Acta Crystallogr.* B **24** 1317–27

[44] Londono J D, Kuhs W F and Finney J L 1993 Neutron-diffraction studies of ice-III and ice-IX on under-pressure and recovered samples *J. Chem. Phys.* **98** 4878–88

[45] Lobban C, Finney J L and Kuhs W F 2000 The structure and ordering of ices III and V *J. Chem. Phys.* **112** 7169–80

[46] Knight C and Singer S J 2006 A reexamination of the ice III/IX hydrogen bond ordering phase transition *J. Chem. Phys.* **125** 064506

[47] Kuo J L 2005 The low-temperature proton-ordered phases of ice predicted by *ab initio* methods *Phys. Chem. Chem. Phys.* **7** 3733–7
[48] Avrami M 1939 Kinetics of phase change. I. General theory *J. Chem. Phys.* **7** 1103–12
[49] Avrami M 1940 Kinetics of phase change. II. Transformation-time relations for random distribution of nuclei *J. Chem. Phys.* **8** 212–24
[50] Avrami M 1941 Kinetics of phase change III. granulation, phase change, and microstructure *J. Chem. Phys.* **9** 177–84
[51] Dewhurst C 2002 Graphical reduction and analysis sans program http://www.ill.fr/lss/grasp
[52] Dewhurst C 2003 Graphical reduction and analysis sans program *Report ILL03DE01T* ILL, Grenoble
[53] Lindner P 2000 Water calibration at D11 verified with polymer samples *J. Appl. Crystallogr.* **33** 807–11
[54] Glatter O and Kratky O 1982 *Small Angle X-ray Scattering* (London: Academic)
[55] Lindner P and Zemb T (ed) 2002 *Neutron, X-Ray and Light Scattering: Introduction to an Investigative Tool for Colloidal and Polymeric Sytems* (Amsterdam: Elsevier)
[56] Arnold G P, Finch E D, Rabideau S W and Wenzel R G 1968 Neutron-diffraction study of ice polymorphs. III. ice Ic *J. Chem. Phys.* **49** 4354–69
[57] Vertsner V N and Zhdanov G S 1966 Electron-microscope study of low-temperature forms of ice *Sov. Phys.—Crystallogr. USSR* **10** 597
[58] Meryman H T 1957 Physical limitations of the rapid freezing method *Proc. R. Soc. Lond.* B **147** 452
[59] Fernandez-Moran H 1960 Low-temperature preparation techniques for electron microscopy of biological specimens based on rapid freezing with liquid helium II *Ann. New York Acad. Sci.* **85** 689–713
[60] Londono J D 1989 *PhD Thesis* University of London
[61] Kobayashi T and Kuroda T 1987 Snow crystals *Morphology of Crystals* ed I Sunagawa (Tokyo: Terra Scientific Publishing) pp 649–743
[62] Onsager L and Runnels L K 1969 Diffusion and relaxation phenomena in ice *J. Chem. Phys.* **50** 1089–103
[63] Kawada S 1978 Dielectric anisotropy in ice Ih *J. Phys. Soc. Japan* **44** 1881